

FIG. 2. (a) Morphological phase diagram in the plane spanned by the strengths of active stress c_a and PS coupling c_{hpa} . (b-f) Snapshots of moving and resting drops [height profile (blue) with overlaid polarization (black) and contact lines (red), grey arrows indicate the direction of motion] at parameters indicated by symbols in (a). Shown is only part of the full computational domain Ω [(b,c) 400×400 , (d-f) 160×160]. The volume $V_{3\text{D}} = 70400$ is fixed in all simulations. (g,h) Velocity dependencies for stationarily moving drops at (g) fixed $c_{\text{hpa}} = 0.035$ and (h) $c_a = -0.04$, at parameters indicated by black lines in (a). A positive [negative] velocity indicates motion parallel [antiparallel] to the drop's mean polarization.

tions for drop motility to emerge and resulting parameter ranges where resting drops, motile drops and unstable drops that undergo splitting occur are studied after presenting our active thin-film model.

The coupled dynamics of film height profile $h(\mathbf{x}, t)$ and height-integrated polarization $\mathbf{P}(\mathbf{x}, t)$ (Fig. 1) is given by [29]

$$\partial_t h = -\nabla \cdot (\mathbf{j}^{\text{Cv}} + \mathbf{j}^{\text{Ca}}) \quad (1)$$

$$\partial_t P_i = -\nabla \cdot [p_i (\mathbf{j}^{\text{Cv}} + \mathbf{j}^{\text{Ca}}) + \mathbf{j}^{\text{DP}_i}] + j_i^{\text{R}}, \quad (2)$$

with the passive fluxes \mathbf{j}^{Cv} , \mathbf{j}^{DP_i} and j_i^{R} derived from a variational principle. The active flux is $\mathbf{j}^{\text{Ca}} = \frac{h^3}{3\eta} \nabla \cdot \boldsymbol{\sigma}^a$ with η denoting viscosity. The active stress tensor is $\boldsymbol{\sigma}^a = -c_a \mathbf{p}\mathbf{p}$ with $c_a > 0$ for extensile and $c_a < 0$ for contractile stress. $\mathbf{p} = \mathbf{P}/h$ denotes the height-averaged polarization.

The energy functional underlying the variational part of the dynamics is

$$\mathcal{F}[h, \mathbf{p}] = \int \left[\frac{\gamma}{2} (\nabla h)^2 + f_w(h) + h f_{\text{spo}}(h, \mathbf{p}^2) + h f_{\text{el}}(\nabla \mathbf{p}) + f_{\text{coupl}}(\nabla h, \mathbf{p}) \right] d\mathbf{x}. \quad (3)$$

It contains capillarity, wettability, spontaneous polarization (double well potential in $\mathbf{p} \cdot \mathbf{p}$) and elasticity of the

polarization field. The final term captures the coupling of bulk polarization and drop surface shape

$$f_{\text{coupl}}(\nabla h, \mathbf{p}) = \frac{c_{\text{hpa}}}{2} \mathbf{p} \cdot \nabla h, \quad (4)$$

and favors at $c_{\text{hpa}} > 0$ an aster-type polarization pattern. Note, that the bulk liquid behavior is governed by nematic order. Only the surface is sensitive to polar order. The complete theoretical framework including self-propulsion and alternative PS couplings (that may lead to vortex-type polarization patterns) is detailed in the Supplementary Material.

Families of resting and steadily moving drops are numerically analyzed using time simulations (finite-element based library `oomph-lib` [30]) and path continuation (`auto07p` [31], `pde2path` [32]) - for details see the Supplementary Material.

Fig. 2(a) summarizes the role of active stress and PS coupling for drop motility and morphology. Passive resting drops at $c_a = 0$ with increasing strength of the PS coupling gradually change between three polarization states: from *uniformly polarized* [$c_{\text{hpa}} = 0$, Fig. 1(a)], to a *boundary aster* state with a half aster-like defect at the contact line [at small $0 < c_{\text{hpa}} < 0.125$, Fig. 1(b)] to a perfectly radial-symmetric *central aster* state with outward pointing polarization [Fig. 2(f)]. The transition results from an increasing dominance of the energy gain due to PS

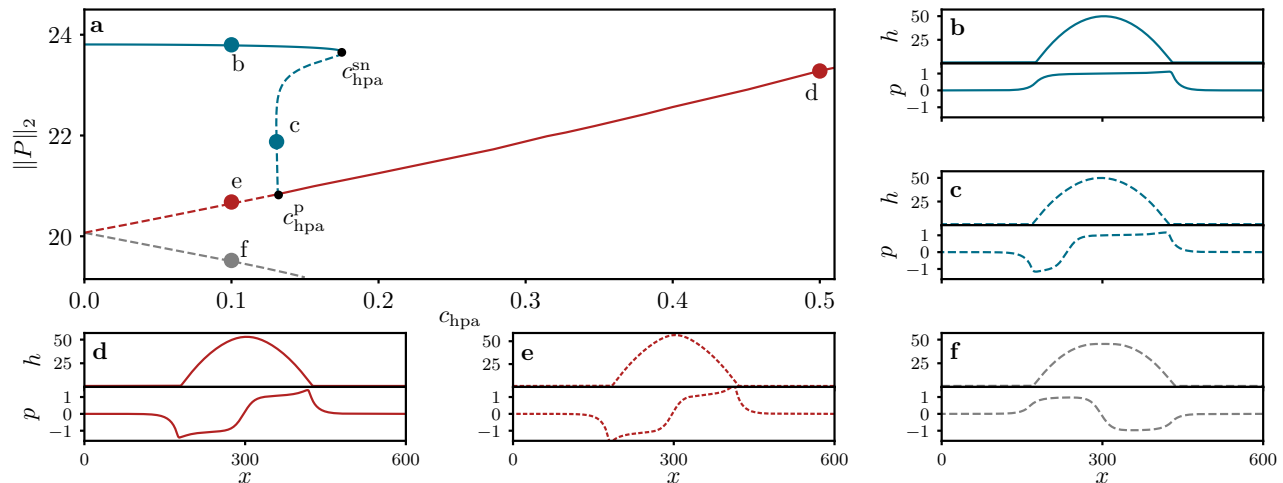


FIG. 3. (a) Drop states in the passive case ($c_a = 0$) are characterized by a bifurcation diagram (L^2 -norm of P over strength of PS coupling c_{hpa}) for polarized ridges with a boundary defect (blue) and a central defect (red and gray). Saddle-node and pitchfork bifurcations are marked by $c_{\text{hpa}}^{\text{sn}}$ and $c_{\text{hpa}}^{\text{p}}$, respectively. (b-f) Height (top) and polarization (bottom) profiles at c_{hpa} values as indicated by symbols in (a). The drop volume is fixed at $V_{2D} = 8280$.

coupling over the energy loss due to a nematic defect in the bulk, i.e. f_{coupl} outweighs f_{el} . This sequence is also essential in the active case ($c_a \neq 0$): There, at $c_{\text{hpa}} = 0$, uniformly polarized drops remain at rest at any active stress, however, deform according to the stress-type. In contrast, at weak surface coupling a back-forth symmetry breaking in drop shape occurs and both, contractile [$c_a < 0$, Fig. 2(d)] and extensile [$c_a > 0$, Fig. 2(e)] active stress, result in steady drop motion. The mechanism of motion is detailed in Fig. 1. The PS coupling destabilizes the uniform polarization field of Fig. 1(a) triggering a symmetry breaking that results in the asymmetric boundary aster of Fig. 1(b). However, the drop maintains a radially symmetric shape. When additionally introducing active contractility the drop qualitatively changes shape as it contracts along the direction of its net polarization. As splay is strongest near the point defect, the drop transiently forms a crescent shape further resulting in the back-forth asymmetric (steady) state shown in Fig. 1(c). The pronounced and weak back-forth asymmetries in the polarization and height profiles, respectively, directly translate into steady drop motion. The defect is located at the trailing edge of the drop [Fig. 2(d)], consistent with results of full 3D hydrodynamic models [16] and the planar case [14, 15].

In contrast, an active extensile stress elongates the drop along the direction of its net polarization. Transiently, liquid is locally accumulated near the defect before the energetic cost of surface and elastic energy reorients the polarization field and forms the steadily moving drop in Fig. 2(e). Note that the advancing drop edge coincides with the location of the defect. Figs. 2(g) and (h) show dependencies of the drop velocity as a function of c_a and

c_{hpa} , respectively, as indicated by straight black lines in Fig. 2(a). The speed monotonously increases with $|c_a|$ and c_{hpa} , respectively.

Interestingly, at stronger PS coupling and active stress large drops are unstable and split into smaller drops, i.e. for $c_a < 0$, the two tails of the mentioned transient crescent form, prolong and split from the main drop, finally resulting in a number of small drops, e.g., Fig. 2(b). For $c_a > 0$ a small drop including the defect splits off leaving the elongated tail behind, see Fig. 2(c). At lower activity $|c_a|$, splitting occurs at larger coupling c_{hpa} . Vice versa at large active stress already a small coupling suffices to overcome the stabilizing surface energy. The splitting process continues until the resulting ensembles of small steadily moving drops only consist of drops sufficiently small for the stabilizing effects to dominate.

Furthermore, at small contractile stresses $c_a < 0$ and strong coupling $c_{\text{hpa}} > 0.125$, we observe resting drops with a central aster defect. Therefore, at small $-0.01 \lesssim c_a < 0$ one may switch between resting and moving drops by only changing the (finite) PS coupling c_{hpa} .

Previously, it has been argued, that splay and bend instabilities in the polarization field are needed to drive drop motion with active stresses [14–16]. Consequently, liquid ridges with a polarization field mainly directed parallel to the 1D substrate should be at rest. Surprisingly, repeating our computations for transversally invariant liquid ridges (2D drops) that show no splay or bend in the polarization reveals qualitatively identical behavior as described above for 3D drops. This allows us to further scrutinize the encountered transitions between resting and moving drops.

Fig. 3(a) shows the bifurcation behavior of passive ridges

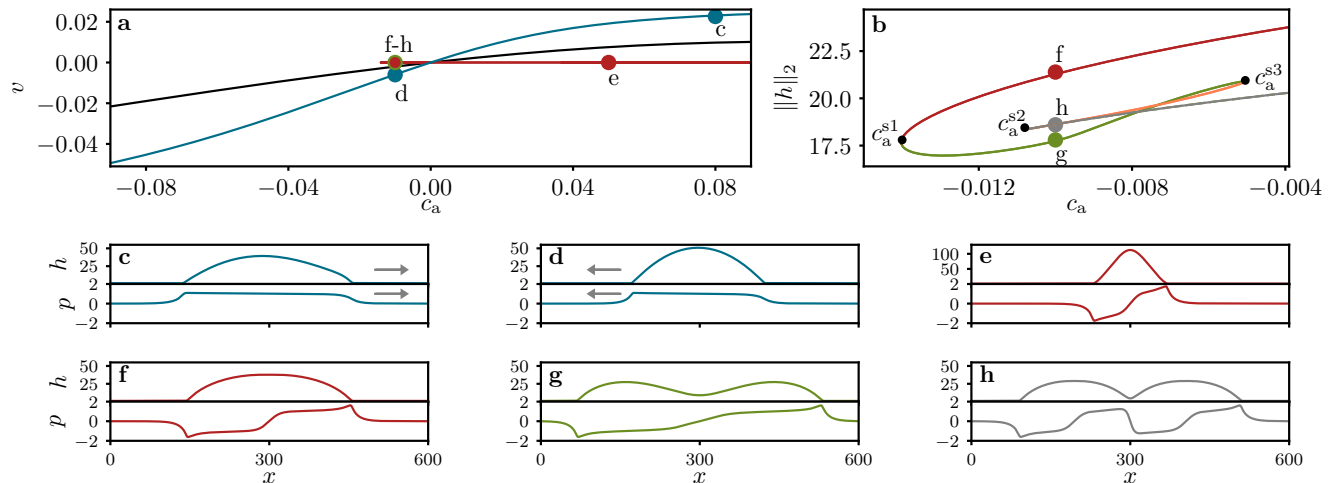


FIG. 4. (a) Velocities v of active polarized ridges with a boundary defect at $c_{\text{hpa}} = 0.1$ (blue) and $c_{\text{hpa}} = 0.035$ (black) and a central defect at $c_{\text{hpa}} = 0.5$ (red) as a function of active stress c_a . (b) Bifurcation diagram related to drop splitting showing the L_2 -norm of height profile over c_a for resting active drops. Labels c_a^{s1} to c_a^{s3} and line styles are explained in the main text. (c-h) Film height (top) and polarization profiles (bottom) at c_a values as indicated by symbols in (a,b). The drop volume is fixed at $V_{2D} = 8280$.

($c_a = 0$) in dependence of the PS coupling c_{hpa} . At small c_{hpa} polarized drops with a boundary defect [Fig. 3(b)] are stable. They lose stability at large c_{hpa} where polarized drops with one central defect are stable [Figs. 3(d), outward pointing polarization], equivalent to the aster structure for the 3D drops above. A central defect drop with inward pointing polarization also exists but is unstable [Fig. 3(f)], so are the states shown in Fig. 3(c,e). Note that the transition between the two stable states shows a hysteresis between c_{hpa}^p and c_{hpa}^{sn} [Fig. 3(a)].

For the stable drops with a boundary defect [at $c_{\text{hpa}} < c_{\text{hpa}}^{sn}$ in Fig. 3(a)], an increase in activity from zero induces without critical stress a steady ridge motion at a velocity comparable to the case of 3D drops in Fig. 2(g), see blue and black curves in Fig. 4(a). The direction of motion depends on the type of active stress and the direction of net polarization, i.e. right polarized drops move to the right [left] at elongational [contractile] stress [Fig. 4(c,d)]. The occurrence of moving ridges evidences a motility mechanism that differs from previously postulated ones [14–16]. Namely, liquid motion results from a spatial modulation of the strength and not the orientation of polarization. Although for 3D drops splay may contribute to the motion, our results for the ridges highlight the polarization strength as primary origin of motility. The similarity of velocities in our 2D and 3D cases indicates a low importance of splay.

It is also very instructive to consider the fate of the passive resting ridges with a central defect in Fig. 3(a) under increasing active stress [Fig. 4(e,f)]: Fig. 4(b) presents a bifurcation diagram showing that these ridges only exist for $c_a > c_a^{s1} = -0.014$. In the vicinity of this critical

stress a complex scenario of drop splitting unfolds: The red branch in Fig. 4(b) consists of the drops with a central defect [e.g. Fig. 4(f)]. This branch annihilates in the saddle-node bifurcation at c_a^{s1} with the green branch of drops with a strong central dip in the height profile [Fig. 4(g)]. At larger c_a^{s3} , the green solid branch annihilates in another saddle-node bifurcation with the orange branch corresponding to drops that are nearly split in two and contain three defects (not shown). Finally, at c_a^{s2} this branch merges with the gray branch, which represents two separated drops each with a central defect [Fig. 4(h)]. This implies that the gray two-drop branch coincides with a branch of single drop states of half the drop volume. The described involved bifurcation scenario for ridges qualitatively corresponds to the transition from a resting aster state to the split moving droplets observed in 3D when increasing the contractile active stress at large PS coupling.

To conclude, we have modeled shallow three-dimensional (3D) active free-surface drops with a mean polar order parallel to the substrate. Incorporating a PS coupling has allowed us to identify a mechanism of motility in which active stresses drive drop motion through spatial variations of polarization strength. Motility is induced even for liquid ridges, implying that splay in the polarization field is not essential for the mechanism. This provides an alternative to previous proposals based on splay or bend [14–16]. The resulting morphological phase diagram for 3D drops is rather rich and well aligned with bifurcation results for ridges (2D drops) that have shed further light on the occurring transitions.

We acknowledge support by the doctoral school “Active living fluids” funded by the German French University (Grant No. CDFA-01-14), and the DAAD & Campus France (PROCOPE 2020 Grant No. 57511756). FS thanks the foundation “Studienstiftung des deutschen Volkes” for financial support.

* u.thiele@uni-muenster.de; <http://www.uwethiele.de>;
ORCID ID: 0000-0001-7989-9271

- [1] G. Gompper, R. G. Winkler, T. Speck, A. Solon, C. Nardini, F. Peruani, H. Löwen, R. Golestanian, U. B. Kaupp, L. Alvarez, *et al.*, *J. Phys.: Condens. Matter* **32**, 193001 (2020).
- [2] M. C. Marchetti, J.-F. Joanny, S. Ramaswamy, T. B. Liverpool, J. Prost, M. Rao, and R. A. Simha, *Rev. Mod. Phys.* **85**, 1143 (2013).
- [3] B. Wallmeyer, S. Trinschek, S. Yigit, U. Thiele, and T. Betz, *Biophys. J.* **114**, 213 (2018).
- [4] S. Douezan, K. Guevorkian, R. Naouar, S. Dufour, D. Cuvelier, and F. Brochard-Wyart, *Proc. Natl. Acad. Sci. U.S.A* **108**, 7315 (2011).
- [5] S. Douezan, J. Dumond, and F. Brochard-Wyart, *Soft Matter* **8**, 4578 (2012).
- [6] O. J. Meacock, A. Doostmohammadi, K. R. Foster, J. M. Yeomans, and W. M. Durham, *Nat. Phys.* **17**, 205 (2021).
- [7] A. Verkhovskiy, T. Svitkina, and G. Borisy, *Curr. Biol.* **9**, 11 (1999).
- [8] C. Pérez-González, R. Alert, C. Blanch-Mercader, M. Gómez-González, T. Kolodziej, E. Bazellieres, J. Casademunt, and X. Trepat, *Nat. Phys.* **15**, 79 (2019).
- [9] H. Morita, S. Grigolon, M. Bock, S. G. Krens, G. Salbreux, and C.-P. Heisenberg, *Dev. Cell* **40**, 354 (2017).
- [10] T. Sanchez, D. T. N. Chen, S. J. DeCamp, M. Heymann, and Z. Dogic, *Nature* **491**, 431 (2012).
- [11] F. Ziebert, S. Swaminathan, and I. S. Aranson, *J. R. Soc. Interface* **9**, 1084 (2012).
- [12] L. Giomi and A. DeSimone, *Phys. Rev. Lett.* **112**, 147802 (2014).
- [13] F. Ziebert and I. S. Aranson, *npj Comput. Mater.* **2**, 16019 (2016).
- [14] S. Marth, V. Wieland, and A. Praetorius, *J. Royal Soc. Interface* **12**, 20150161 (2015).
- [15] E. Tjhung, D. Marenduzzo, and M. E. Cates, *Proc. Natl. Acad. Sci. U. S. A* **109**, 12381 (2012).
- [16] E. Tjhung, A. Tiribocchi, D. Marenduzzo, and M. E. Cates, *Nat. Commun.* **6**, 5420 (2015).
- [17] A. Oron, S. Davis, and S. Bankoff, *Rev. Mod. Phys.* **69**, 931 (1997).
- [18] S. Sankararaman and S. Ramaswamy, *Phys. Rev. Lett.* **102**, 118107 (2009).
- [19] J. F. Joanny and S. Ramaswamy, *J. Fluid Mech.* **705**, 46 (2012).
- [20] D. Khoromskaia and G. P. Alexander, *Phys. Rev. E* **92**, 062311 (2015).
- [21] G. Kitavtsev, A. Münch, and B. Wagner, *Proc. R. Soc. A* **474**, 20170828 (2018).
- [22] A. Loisy, J. Eggers, and T. B. Liverpool, *Phys. Rev. Lett.* **123**, 248006 (2019).
- [23] A. Loisy, J. Eggers, and T. B. Liverpool, *Soft Matter* **16**, 3106 (2020).
- [24] H. Wang, T. Qian, and X. Xu, *Soft Matter* **17**, 3634 (2021).
- [25] B. M. Amar and L. J. Cummings, *Phys. Fluids* **13**, 1160 (2001).
- [26] T.-S. Lin, L. J. Cummings, A. J. Archer, L. Kondic, and U. Thiele, *Phys. Fluids* **25**, 082102 (2013).
- [27] T.-S. Lin, L. Kondic, U. Thiele, and L. J. Cummings, *J. Fluid Mech.* **729**, 214 (2013).
- [28] P.-G. De Gennes, *Rev. Mod. Phys.* **57**, 827 (1985).
- [29] S. Trinschek, F. Stegemerten, K. John, and U. Thiele, *Phys. Rev. E* **101**, 062802 (2020).
- [30] M. Heil and A. L. Hazel, in *Fluid-Structure Interaction: Modelling, Simulation, Optimisation*, edited by H.-J. Bungartz and M. Schäfer (Springer, Berlin, Heidelberg, 2006) pp. 19–49.
- [31] H. A. Dijkstra, F. W. Wubs, A. K. Cliffe, E. Doedel, I. F. Dragomirescu, B. Eckhardt, A. Y. Gelfgat, A. Hazel, V. Lucarini, A. G. Salinger, E. T. Phipps, J. Sanchez-Umbria, H. Schuttelaars, L. S. Tuckerman, and U. Thiele, *Commun. Comput. Phys.* **15**, 1 (2014).
- [32] H. Uecker, D. Wetzel, and J. Rademacher, *Numer. Math.-Theory Methods Appl.* **7**, 58 (2014).